Continuum Modeling of Inductor Hysteresis and Eddy Current Loss Effects in Resonant Circuits

Jason Pries, *Member, IEEE*
Oak Ridge National Laboratory
Oak Ridge, TN
priesjl@ornl.gov

Lixin Tang, *Member, IEEE*
Oak Ridge National Laboratory
Oak Ridge, TN
tangl@ornl.gov

Tim Burress, *Member, IEEE*
Oak Ridge National Laboratory
Oak Ridge, TN
burressta@ornl.gov

Abstract—This paper presents experimental validation of a high-fidelity toroid inductor modeling technique. The aim of this research is to accurately model the instantaneous magnetization state and core losses in ferromagnetic materials. Quasi–static hysteresis effects are captured using a Preisach model. Eddy currents are included by coupling the associated quasi-static Everett function to a simple finite element model representing the inductor cross sectional area. The modeling technique is validated against the nonlinear frequency response from two different series RLC resonant circuits using inductors made of electrical steel and soft ferrite. The method is shown to accurately model shifts in resonant frequency and quality factor. The technique also successfully predicts a discontinuity in the frequency response of the ferrite inductor resonant circuit.

I. INTRODUCTION

The macroscopic electromagnetic characteristics of ferromagnetic materials are the result of a set of intertwined phenomena occurring at several different length scales [1]–[3]. Predicting losses in ferromagnets can greatly aid in the design and optimization of electric components such as transformers, resonant circuits, and electric machines. An overview of core losses and their physical origins can be found in [4]. Nonlinear amplitude variation, phase shifts, harmonic generation, and damping all greatly impact the accuracy of simulated resonant behavior compared to linear circuits. Unfortunately, simulating whole magnetic materials by fully coupling atomistic, domain, and bulk material scale phenomena is still a difficult problem on today's most powerful supercomputers.

Purely mathematical models of macroscopically observed hysteresis exists independently – although often inspired by – the physical origins of magnetic hysteresis [5]. These methods abstract away some details of the atomistic and domain scales while guaranteeing certain model characteristics and accuracy when identified from suitable experimental data. Mathematical models also permit separating quasi–static hysteresis behavior from the high–frequency eddy current phenomenon. It has

been demonstrated that quasi-static scalar models of hysteresis may be extended to include frequency dependent effects based on suitable analysis of Faraday's law [6].

Most investigations into coupled hysteresis/resonant circuit models have focused on ferro-resonant phenomenon observed in transformers. A parametric Preisach function was used to study the existence of bifurcations leading to a subharmonic resonant solution in an RLC circuit [7]. The authors noted this behavior was not apparent in models with single-valued magnetization curves. They raised a note of skepticism about using non-hysteretic inductor characteristic in the analysis of even the simplest of ferro-resonant circuits. Subsequently, a more detailed model including eddy currents was used to examine parameter dependent bistable operating regions [8]. A comparative study showed that models with similar major loops can respond quite differently with respect to their ability to capture noise-induced resonance [9]. This emphasizes the need to carefully validate models in the context of the phenomenon under investigation.

This paper presents a sequence of mathematical techniques and experimental measurements which are composed to construct and validate high-fidelity inductor models. The sequence begins with a set of quasi-static major loop measurements used to identify a Preisach model to represent the quasi-static hysteresis behavior. Next, core geometry and material conductivity are used to construct a finite-element model which captures eddy currents at higher frequencies. Finally, a method for coupling field based inductor models to a simple series RLC circuit is demonstrated. Simulations accurately track measured changes in resonant frequency and quality factor as source amplitude and frequency are varied. The model also successfully predicts a measured discontinuity in the frequency response of one of the resonant circuit.

II. HYSTERESIS

The quasi-static hysteresis characteristics of ferromagnetic toroid inductors can be accurately modeled using a scalar Preisach model. Identifying such models requires measuring major hysteresis loops over a range of peak flux-density values. The measurements must be taken at a frequency low enough such that the loops appear constant with respect to reasonable frequency variations. This requirement ensures that eddy currents have a negligible effect on the observed macroscopic
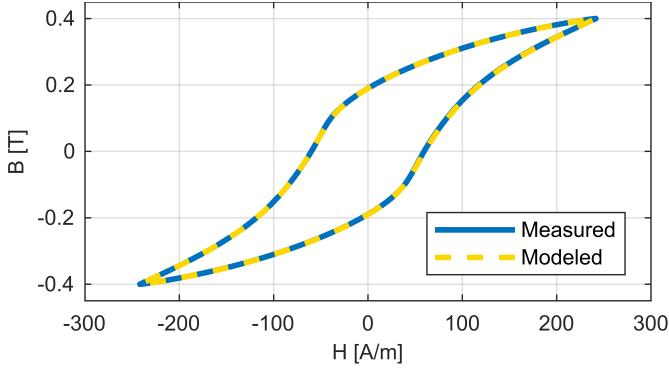
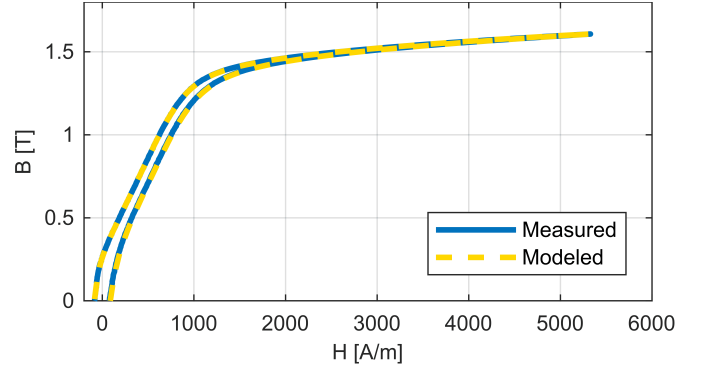Fig. 1. M19 hysteresis loop with a 400mT amplitude measured at 5Hz

Fig. 2. M19 hysteresis loop with a 1.6T amplitude measured at 5Hz

hysteresis loops. The required measurement frequency range can be determined by requiring that the skin-depth of the inductor material is much larger than the height and radial width of core.

We assume the core material has associated with it a nonlinear function describing the relationship between field-intensity H and flux-density B given by

$$B = \mu_o (H + M (H)). \quad (1)$$

The magnetization state M of the core represents the nonlinear part of the B-H relationship. The value $\mu_o M$ is referred to as the magnetic polarization. Assume we have taken a set of major loop measurements $(H_m(t), M_m(t))$ at a frequency $f = 1/T$. For simplicity, we assume the ascending branch of the hysteresis loop occurs for $t \in [0, T/2]$ and the descending branch for $t \in [T/2, T]$. The minimum and maximum values of $M_m(t)$ occur at $t = 0$ and $t = T/2$, respectively.

The scalar Preisach model assumes the output state of a material exhibiting hysteresis can be described as an integral over a two-dimensional space describing the internal state of a distribution of hysterons (i.e. two state relays). Let $\gamma_{\alpha,\beta}$ be the hysteron which switches to a value of $+1.0$ for $x > \alpha$ and -1.0 for $x < \beta$. The output of the Preisach hysteresis model with density function $\mathcal{P}$ is given by

$$y = \int_{\mathcal{S}_+} \mathcal{P}(\alpha,\beta)\, d\alpha d\beta - \int_{\mathcal{S}_-} \mathcal{P}(\alpha,\beta)\, d\alpha d\beta, \quad (2)$$

where $\mathcal{S}_+$ is the set of all (α,β) such that $\gamma_{\alpha,\beta} = +1.0$ and $\mathcal{S}_-$ is the set of all (α,β) such that $\gamma_{\alpha,\beta} = -1.0$. A hysteron with $\beta > \alpha$ is typically thought to be nonphysical for ferromagnetic materials and $\mathcal{P}(\alpha,\beta) = 0$ is assumed in this region. The asymmetric switching of individual hysterons gives rise to internal memory and is the cause of hysteresis observed on a macroscopic scale. The continuous distribution of hysterons ensures a smooth output variation with the applied field [5].

Direct determination of $\mathcal{P}$ is difficult due to the need to twice differentiate noisy experimental data. However, the measured major hysteresis loop ascending and descending

branches can be transformed directly into an equivalent Everett function model. The Everett function $\mathcal{E}(\alpha,\beta)$ is given by

$$\mathcal{E}(H_m(0), H_m(t)) = M_m(t) - M_m(0), \quad (3)$$

for the ascending branch with $t \in [0, T/2]$ and

$$\mathcal{E}(H_m(T/2), H_m(t)) = M_m(t) - M_m(T/2) \quad (4)$$

for the descending branch descending with $t \in [T/2, T]$. In words, the line (x, y) described by $y = \mathcal{E}(h, x)$ for $h > 0$, $x \in [-h, h]$ is exactly the ascending hysteresis loop branch measured for the peak field h, shifted up by the corresponding peak magnetization. The Preisach density function can be calculated from the Everett function as

$$\mathcal{P} = -\frac{\partial^2 \mathcal{E}}{\partial \alpha \partial \beta}. \quad (5)$$

The material state of a scalar Preisach system is completely described by a set of past input extrema. The line defined by $\mathcal{L}(t) = \mathcal{S}_+ \bigcap \mathcal{S}_-$ associated with the waveform $H(\tau)$ for $\tau \in [0, t]$ is composed of a set of horizontal and vertical lines (or links) whose vertices generate a sequence of N_n values $\{H^n\}$. Using this sequence, the magnetization state at time t is given by

$$M = -\frac{1}{2}\mathcal{E}(-H^{max}, H^{max}) + \sum_{n=1}^{N_n-1} \mathcal{E}(H^n, H^{n+1}), \quad (6)$$

where $H^{N_n} = H(t)$ and H^{max} is the maximum absolute value of $\{H^n\}$. The exact method required to track the evolution of $\mathcal{L}(t)$ given $H(\tau)$ is described in [5].

A sample of measured and experimental hysteresis loops are given in Fig. 1 and Fig. 2 for a toroid core constructed of several sheets of M19 electrical steel. The measurements were taken at 5Hz to minimize frequency dependent effects. The experimental hysteresis loop data was filtered to remove noise and Bézier splines are used to interpolate the Everett function between measured values. At both low and high flux-density levels, the Everett function faithfully reproduces the measured behavior.
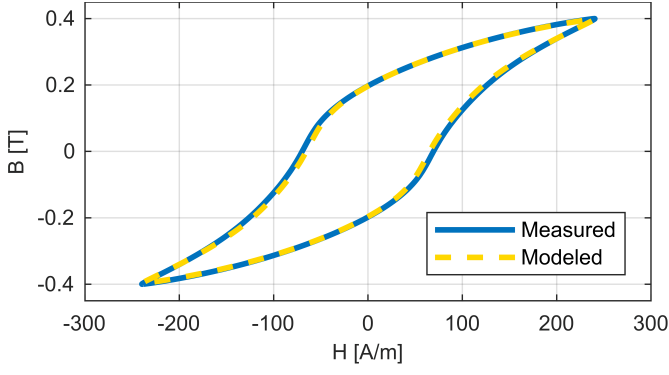
Fig. 3. M19 hysteresis loop with a 400mT amplitude measured at 50Hz

Fig. 4. M19 hysteresis loop with a 400mT amplitude measured at 500Hz

III. EDDY CURRENTS

The macroscopically observed B-H loops of ferromagnetic materials are known to widen as excitation frequency increases. This is due to the development of eddy currents in the material body as the skin depth decreases below the smallest dimension of the sample perpendicular to the field direction. This phenomenon is not hysteresis – it appears in non-magnetic materials such as copper – but *is* an additional source of core losses. To a first approximation, quasi-static hysteresis loops can be considered a property of the bulk material while the way the loops widen with frequency depends on the geometry of the sample.

The main equations used to describe the field dynamics in this work are Ampere's law,

$$\nabla \times \vec{H} = \vec{J}, \tag{7}$$

and Faraday's law,

$$\nabla \times \vec{E} = -\frac{\partial \vec{B}}{\partial t}. \tag{8}$$

Toroidal cores can be modeled in axisymmetric coordinates with H_θ and B_θ the only non-zero components of the field-intensity and flux-density, respectively. Restricting our attention to the interior of the core and assuming ohmic conduction,

$$\vec{J} = \sigma \vec{E}, \tag{9}$$

with material conductivity σ, we may rewrite Ampere's law,

$$\sigma E_r = -\frac{\partial H_\theta}{\partial z}, \tag{10}$$

$$\sigma E_z = \frac{1}{r}\frac{\partial r H_\theta}{\partial r}, \tag{11}$$

and Faraday's law,

$$-\frac{\partial B_\theta}{\partial t} = \frac{\partial E_r}{\partial z} - \frac{\partial E_z}{\partial r}. \tag{12}$$

Combining (10)-(12) gives

$$\sigma \frac{\partial B_\theta}{\partial t} = \frac{\partial^2 H_\theta}{\partial z^2} + \frac{\partial}{\partial r}\frac{1}{r}\frac{\partial r H_\theta}{\partial r}, \tag{13}$$

which is simply the non-linear diffusion equation

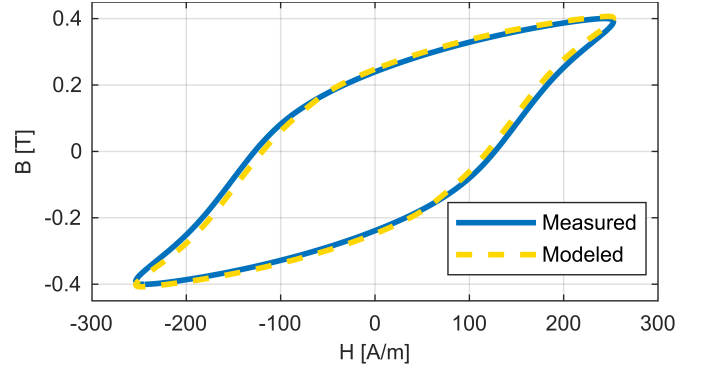$$\sigma \frac{\partial B_\theta}{\partial t} = \nabla^2 H_\theta \tag{14}$$

in axisymmetric coordinates.

Equation (13) is solved using finite element analysis. Given shape functions w_i, the corresponding weight functions are chosen to be $r w_i$. Multiplying (13) by $r w_i$ and integrating over the core cross section Ω gives

$$\int_\Omega r w_i \sigma \frac{\partial B_\theta}{\partial t} dr dz = \int_\Omega r w_i \frac{\partial^2 H_\theta}{\partial z^2} dr dz \\ + \int_\Omega r w_i \frac{\partial}{\partial r}\frac{1}{r}\frac{\partial r H_\theta}{\partial r} dr dz. \tag{15}$$

The domain $\Omega = [r_{id}, r_{od}] \times [-h_z/2, h_z/2]$ where r_{id} and r_{od} are the inner and outer radius, respectively, and h_z is the core height. Using integration by parts on (15) and expanding the partial derivatives with respect to r reveals the corresponding symmetric weak form:

$$\int_\Omega w_i \sigma \frac{\partial B_\theta}{\partial t} r dr dz + \int_\Omega \frac{\partial w_i}{\partial z}\frac{\partial H_\theta}{\partial z} r dr dz \\ + \int_\Omega \left(\frac{\partial w_i}{\partial r} + \frac{w_i}{r}\right)\left(\frac{\partial H_\theta}{\partial r} + \frac{H_\theta}{r}\right) r dr dz = 0. \tag{16}$$

The field solution is approximated as

$$H_\theta(r, z) = \sum_j w_j H_j, \tag{17}$$

where H_j are the interpolated field-intensity values for node j. Our implementation utilizes a single element and a high–order polynomial basis to obtain an accurate field representation.

The integrals in (16) are evaluated using numerical quadrature with quadrature points (r_q, z_q), quadrature weights ω_q, and is advanced in time using the implicit-Euler method. Before application of boundary conditions, this yields the following equation:

$$F\frac{B^k - B^{k-1}}{\Delta t} + KH^k = 0. \tag{18}$$

The vector $H^k = \{H_j^k\}$ contains the nodal field-intensity values. The vector $B^k = \{B_q^k\}$ contains flux-density values at the quadrature points which are generally different from the node locations. The entries of the matrix F are the values

of the integrand of the first term in (16) evaluated at the quadrature points and multiplied by the quadrature weights;

$$F_{i,q} = \sigma w_{i,q} r_q \omega_q. \tag{19}$$

The entries of the matrix K are given by

$$K_{i,j} = \sum_q \frac{\partial w_{i,q}}{\partial z} \frac{\partial w_{j,q}}{\partial z} r_q \omega_q \\ + \left(\frac{\partial w_{i,q}}{\partial r} + \frac{w_{i,q}}{r_q} \right) \left(\frac{\partial w_{j,q}}{\partial r} + \frac{w_{j,q}}{r_q} \right) r_q \omega_q. \tag{20}$$

The notation $w_{i,q}$ is used to indicate the value of the function w_i (or its partial derivative) evaluated at quadrature point q.

The discretized problem is advanced in time by solving the nonlinear equation using Newton's method. To do this, it is necessary to calculate the differential permeability μ_q from the slope of the active branch of the hysteresis loop at the quadrature points. This is done by directly evaluating the first partial derivative of the Everett function:

$$\mu_q = \frac{\partial B_q}{\partial H_q} = \mu_o \left[1 + \frac{\partial \mathcal{E}}{\partial \beta} \left(H_q^{N-1}, H_q^k \right) \right]. \tag{21}$$

where $H_q^{N_m-1}$ are the quadrature point link values associated with $\mathcal{L}$ described in Section II and $H_q^{N_m} = H_q^k$. Following linearization, entries of the Jacobian $\mathcal{J}$ are given by the following expression:

$$\mathcal{J}_{i,j} = K_{i,j} + \sum_q \frac{\sigma \mu_q}{\Delta t} w_i w_j r_q \omega_q. \tag{22}$$

Dirichlet boundary conditions are applied by assuming the current in the inductor winding applies a field-intensity to the boundary of the core. Let H_Γ^k be the values of H^k on the boundary of Ω. When $H_j^k \in H_\Gamma$, the value is prescribed by the applied primary current I^k;

$$H_j^k = \frac{N_t}{2\pi r_j} I^k, \tag{23}$$

where N_t is the number of turns, and r_j is the radius of node j. After application of the boundary conditions, (18) becomes

$$F_d \frac{B^k - B^{k-1}}{\Delta t} + K_d H^k = D I^k. \tag{24}$$

The matrices F_d and K_d are adapted from F and K, respectively, by setting the rows associated with the core boundary values to zero, except the corresponding diagonal entries of K which become 1. The vector D translates the forcing current I^k into the boundary field values using (23). The relationship between the winding current and the field boundary values provides a mechanism for coupling the field equations to circuit models as described in the next section.

The loop widening phenomena is demonstrated on the M19 toroid for an excitation frequency of 50Hz in Fig. 3 and 500Hz in Fig. 3. Compared to the 5Hz loop shown in Fig. 1, the 50Hz loop is nearly unchanged. On the hand, the 500Hz loop encloses a significantly larger area, indicating an increase of losses per cycle. Observe in Fig. 4 that for

a fixed flux-density amplitude, the apparent coercivity of the material increases. Appendix A briefly outlines a method for determining the effective material conductivity given a set of apparent coercivity measurements at different frequencies.

IV. RESONANT CIRCUIT COUPLING

A series RLC resonant circuit with a nonlinear inductor can be described by a set of ordinary differential equations;

$$I - C \frac{\partial V_c}{\partial t} = 0, \tag{25}$$

$$\frac{\partial \lambda}{\partial t} + RI + V_c = V_s(t). \tag{26}$$

The voltage induced by the flux in the core is modeled as a nonlinear flux-linkage λ which is implicitly a function of H. The induced voltage can be written as the integral of the time derivative of B over Ω scaled by the number of turns N_t and – in the case of laminated cores – the number of laminations N_l:

$$\frac{\partial \lambda}{\partial t} = N_t N_l \int_\Omega \frac{\partial B}{\partial t} dr dz. \tag{27}$$

This allows the circuit equations to be driven by the continuum field model in Section III. After discretizing in time, we arrive at the following equations;

$$I^k = C \frac{V_c^k - V_c^{k-1}}{\Delta t}, \tag{28}$$

$$S \frac{B^k - B^{k-1}}{\Delta t} + R I^k + V_c^k = V_s(t^k). \tag{29}$$

The vector S is a discrete version of the integral operator in (27) with entries given by

$$S_q = N_t N_l \omega_q. \tag{30}$$

The solution is advanced in time using Newton's method to solve the coupled field-circuit equations represented by (24), (28), and (29). Doing this requires linearizing the first term in (29) with respect to the field-intensity. The corresponding entries of the Jacobian are given by $\mathcal{J}_{\lambda,j}$:

$$\mathcal{J}_{\lambda,j} = N_t N_l \sum_q \frac{u_q}{\Delta t} w_j \omega_q. \tag{31}$$

V. EXPERIMENTAL RESULTS

We now compare the accuracy of the two different models constructed using the proposed technique. The first inductor is constructed of M19 electrical sheet steel laminations and is deployed in a circuit operating at resonance near 200Hz. The second is a ferrite toroid of T38 ferrite material by TDK in a circuit operating at resonance near 10kHz. We focus our attention on how the models capture shifts in the resonant frequency and quality factor since these values depend critically on nonlinear the inductance and losses.

TABLE I
M19 INDUCTOR RESONANT CIRCUIT PROPERTIES

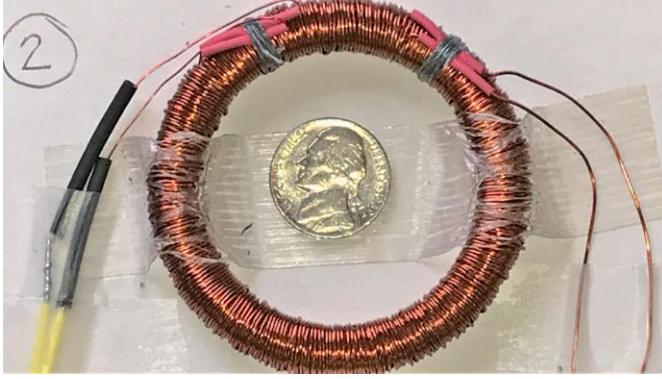| I.D.	O.D.	Height	σ	Turns	R_{dc}	C
62.1mm	50.8mm	5.31mm	4.1MS/m	460	1.1Ω	9.88μF

Fig. 5. M19 toroid inductor

A. M19 Electrical Steel Core

The first circuit utilizes an inductor with made of M19 electrical steel. The core consists of a stack of 15 laminations each approximately 0.35mm thick. The inductor as wound is depicted in Fig. 5. The core was originally designed to conform to the ASTM A773 / A773M-01 ring core standard [10]. A 10μF capacitor was chosen to locate the resonant frequency of the system near 200Hz based on a representative inductance value. Table I lists the key measured inductor and resonant circuit characteristics. The measured M19 Everett function is depicted in Fig. 6.

The voltage source amplitude was swept from 1V_{rms} to 4V_{rms}. The source frequency was swept from 50Hz to 500Hz. The simulated and measured values of the capacitor and inductor RMS voltages are shown in Fig. 7 and Fig. 8, respectively. The inductor voltage was measured across the primary winding and reflects the sum of the real and reactive parts of the voltage drop: The primary voltage drop is indicative of the apparent inductance, winding resistance, and core losses.

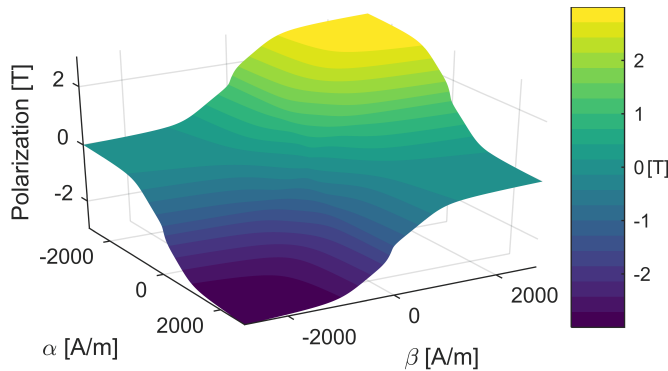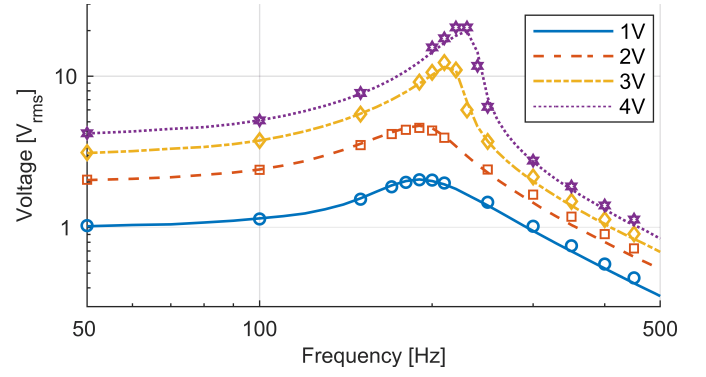The simulation results capture several important trends

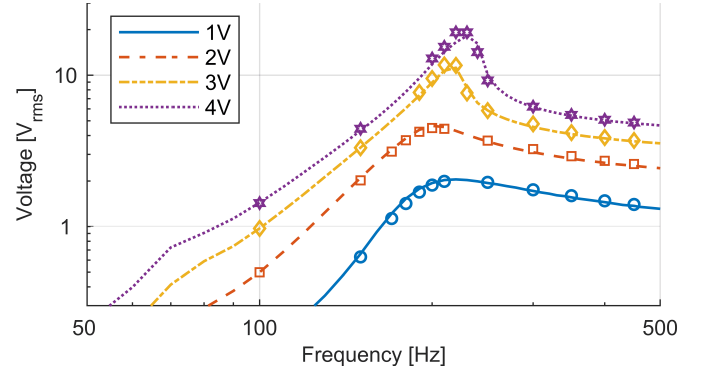Fig. 7. Simulated (lines) and measured (points) RMS capacitor voltage in the M19 resonant circuit

Fig. 8. Simulated (lines) and measured (points) RMS inductor primary voltage in the M19 resonant circuit
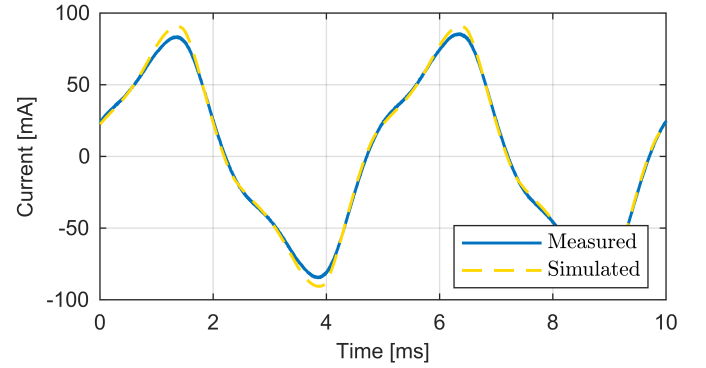

Fig. 9. Current waveforms for the 2Vrms sinusoidal input at 200Hz

observed in the experimental results related to location of the resonant peak and changes in the quality factor. The resonant peak is observed to shift from 190Hz at 1V_{rms} input to 230Hz at 4V_{rms}. The measured quality factor – determined as the ratio of input voltage to capacitor voltage – shifts from 2.07 to 5.26 at these points, versus the predicted values of 2.08 and 4.97. A comparison of simulated and measured current at 2V_{rms} and 200Hz in Fig. 9 demonstrates successful prediction of a non-sinusoidal waveform.

Fig. 6. Measured Everett function for the M19 toroid

TABLE II
T38 INDUCTOR RESONANT CIRCUIT PROPERTIES

I.D.	O.D.	Height	σ	Turns	R_{dc}	C
13.7mm	22.1mm	7.90mm	120S/m	22	60mΩ	69.1nF

Fig. 10. T38 toroid inductor

B. T38 Ferrite Toroid

The second circuit is designed with a ferrite toroid core using TDK's T38 material. The target resonant frequency of this circuit was chosen to be 10kHz. The core size and material were chosen so that the skin-depth of the material at 10kHz – based on data sheet information – is approximately equal to two times the core height at 10kHz. This ensures that eddy currents are an appreciable part of the total circuit losses. Otherwise, a comparison would only judge the quasi-static model accuracy and have little to do with the dynamic behavior. The core was wound with 26AWG magnet wire so that the copper losses should be nearly frequency independent over the range of measured frequencies. The relevant inductor and capacitor properties are listed in Table II.

The Everett function identified using this core is shown in Fig. 11. The measured capacitor and primary inductor RMS voltages are shown in Fig. 12 and Fig. 13, respectively. The source voltage amplitude is swept from 1V$_{rms}$ to 3V$_{rms}$. The source frequency is swept between 4kHz and 20kHz. Again, good agreement between the simulated and measured trends
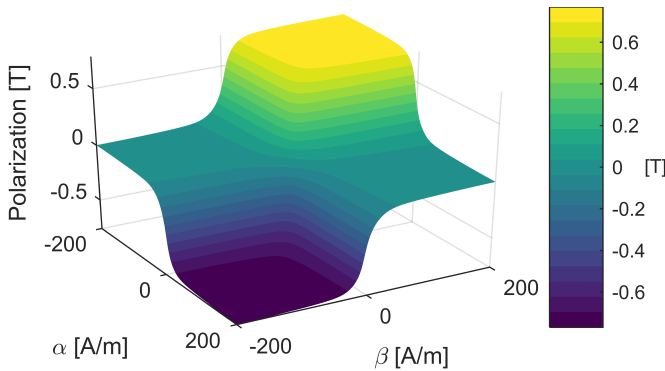

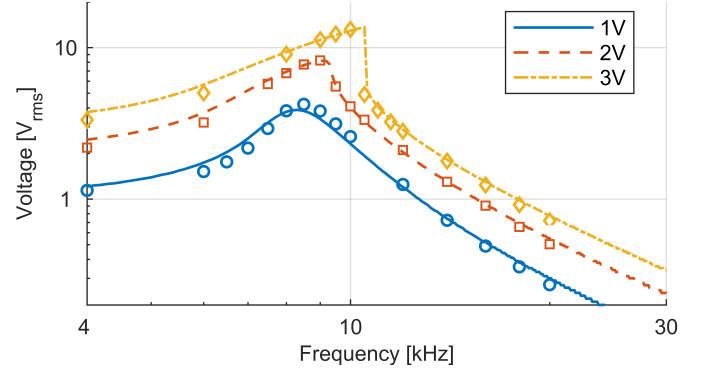Fig. 11. Measured Everett function for the T38 ferrite core

Fig. 12. Simulated (lines) and measured (points) RMS capacitor voltage in the T38 resonant circuit
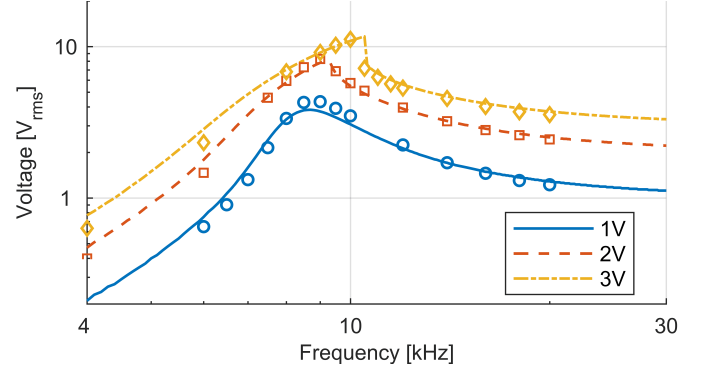

Fig. 13. Simulated (lines) and measured (points) RMS primary inductor voltage in the T38 resonant circuit

are observed. The capacitor voltage gain at a source amplitude of 1V$_{rms}$ and frequency of 8.5kHz is measured to be 3.82 versus a predicted value of 4.22. At a source amplitude of 3V$_{rms}$ and frequency of 10kHz, the measured capacitor gain increases to 4.31 versus a predicted value of 4.40.

The apparent discontinuity in frequency response for the 3V$_{rms}$ source amplitude near 10kHz is discussed further in Section V-B1. Overall, the discrepancies are somewhat larger for the 1V$_{rms}$ source input amplitude than the others. The reasons for this are explored more in Section VI. Notably, it is likely the modeled hysteresis characteristic is less accurate at low flux levels due to the small core size.

1) Steady–State Periodic Orbits Discontinuity: The resonant circuit can be viewed as a dynamic system described by the nonlinear equation

$$\frac{\partial x}{\partial t} = f\left(x\,;v_s, f_s\right), \qquad (32)$$

where $x = \{i, v\}$ is the state vector consisting of the inductor current and capacitor voltage, and v_s and f_s are system parameters describing the source applied voltage and frequency, respectively. Under reasonable assumptions on the initial conditions of the system, the solutions of (32) tend toward periodic orbits $x = \Phi\left(t\,;v_s, f_s\right)$ with

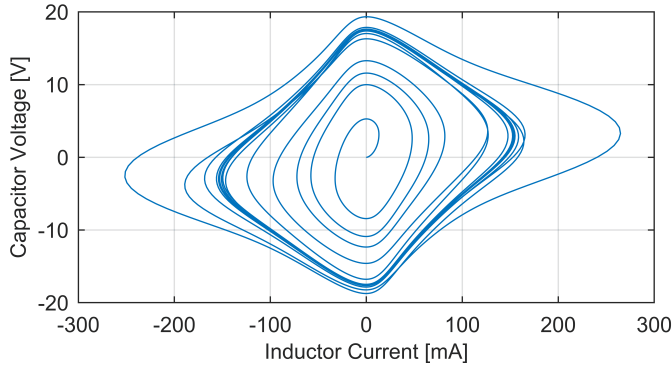$$\Phi\left(t\,;v_s, f_s\right) = \Phi\left(t + T_s\,;v_s, f_s\right), \qquad (33)$$

Fig. 14. Phase portrait of the T38 RLC resonant circuit operated at $3V_{rms}$ source amplitude and 10.5kHz source frequency
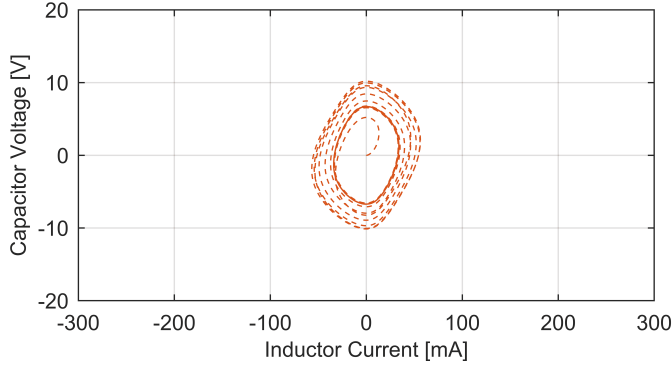

Fig. 16. Comparison of the initial phase portrait transients for 10.5kHz and 10.7kHz source frequency

Fig. 15. Phase portrait of the T38 resonant circuit operated at $3V_{rms}$ source amplitude and 10.7kHz source frequency
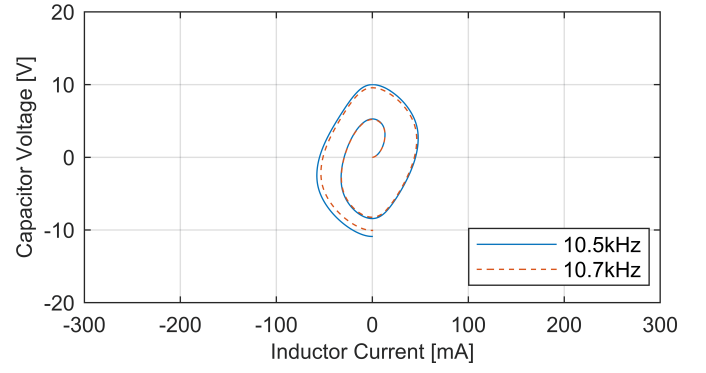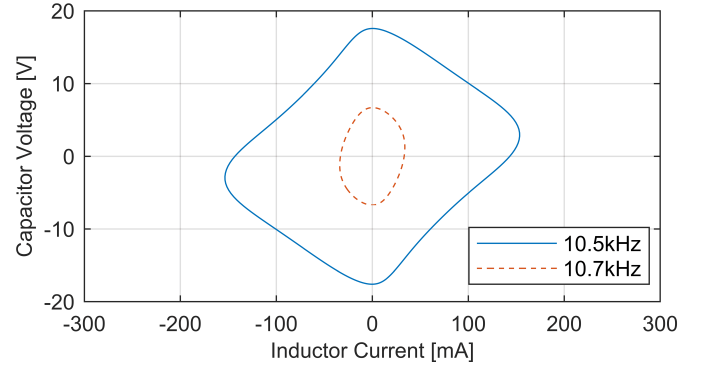

Fig. 17. Comparison of the steady–state orbits of the phase portrait for 10.5kHz and 10.7kHz source frequency

and $T_s = 1/f_s$. Examining, for example, the $3V_{rms}$ applied voltage data in Fig. 12, a discontinuous change of the capacitor voltage is observed as the source frequency is varied near 10.5kHz. This is observable as a discontinuous change in the steady-state periodic orbit Φ as f is varied.

Fig. 14 and Fig. 15 show simulated phase portraits for the T38 resonant circuit at 10.5kHz and 10.7kHz, respectively. Both portraits begin at the origin and overshoot before ultimately settling into their respective periodic orbits. A comparison of the initial transient portion of the portraits are shown Fig. 16, which are observed to be quite close. The steady–state phase portraits are shown in Fig. 17.

The occurrence of the discontinuity can be understood by examining opposing positive and negative feedback effects in the resonant circuit. Start by consider the system at a very low frequency. An effective inductance can be calculated around a nominal current trajectory and, along with the capacitor value, an apparent resonant frequency. Increasing the frequency slightly moves the system toward this apparent resonant peak. This will cause the inductor current to increase, pushing it closer to saturation, lowering the effective inductance, and further increasing the apparent resonant frequency.

As the frequency is varied in this way the system is, in a sense, chasing the resonant peak. However, inductor losses and therefore system damping also increase with fre-

quency. Above the discontinuity frequency, the damping is large enough so that the system can no longer escape to the low inductance (high current) orbit and the apparent resonant frequency exhibits a step decrease. This is evident from the phase portrait transient in Fig. 16. At first, the 10.7kHz spiral remains bounded by but near the 10.5kHz spiral. After the initial transient, the 10.5kHz portrait continues to increase its distance from the origin while damping at 10.7kHz prevents the system from increasing its amplitude any further. Thus, the portrait associated with the 10.7kHz source frequency ultimately decays to a smaller amplitude orbit.

VI. Future Work

There are several known sources of error in the cores models – particularly the T38 core – which may explain some of the discrepancies between the simulations and experiments. First, the T38 core is much smaller and has fewer number of turns than the M19 core, which naturally introduces more uncertainty into the magnetic characterization process, especially at low field levels. This could be alleviated by using a larger toroid to gather material property data for simulating smaller cores. This introduces the question of material property variability which must nonetheless be examined if the technique laid out here is to be used as a prognostic tool.

Second, the standard ferrite core dimensions as described by the International Magnetics Association's IMA-STD-140 are

not compatible with the dimensions required by the ASTM A773 / A773M-01 ring core standard [11]: The ASTM requires, approximately, ratio of mean core diameter to core thickness of greater than 10 to 1. This is, presumably, to limit the radial variation of the magnetic field-intensity in the core to a range small enough so that any error can effectively be averaged out. Standard ferrite toroid cores have a ratio closer to 4 to 1, making them more susceptible to this systematic error. ASTM standard conforming toroids could be fabricated at some expense.

Finally, ferrite toroids have filleted corners which locally influence the field shape and losses. Similarly, the M19 inductor was modeled under the assumption that each lamination experiences identical field and current distributions. These issues can be resolved by generalizing the finite-element portion of the technique to allow individual elements per lamination and geometrically mapped elements to handle filleted corners [12].

VII. Conclusion

This paper presented a technique for high-fidelity modeling of toroid inductor magnetic and core loss properties along with experimental results validating the method. Two different cores were examined in the context of series RLC resonant circuits; one made from M19 electrical steel laminations and one ferrite core suitable for operation in the 10kHz frequency range. Good agreement between simulation and experimental results was observed: The models demonstrated an ability to predict changes in the location of the circuit's resonant peak and associated quality factor, indicating an accurate representation of nonlinear inductance and losses over a wide range of input voltages and frequencies. The model also successfully predicted a discontinuity in the frequency response of one of the resonant circuits resulting from opposing positive and negative feedback interactions caused by the interaction of magnetic saturation and core losses.

Acknowledgments

Appendix
Estimation of Effective Core Conductivity from Frequency Dependent Coercivity

The effective conductivity of the core material is a difficult parameter to assess for model construction but is essential for accurately modeling eddy current core losses. It was noted in Section III that, for a fixed peak flux-density magnitude, the apparent coercivity of the material is observed to increase with frequency. The increase is directly related to the material conductivity as eddy currents in the core are the cause of this phenomenon. This knowledge provides a mechanism for
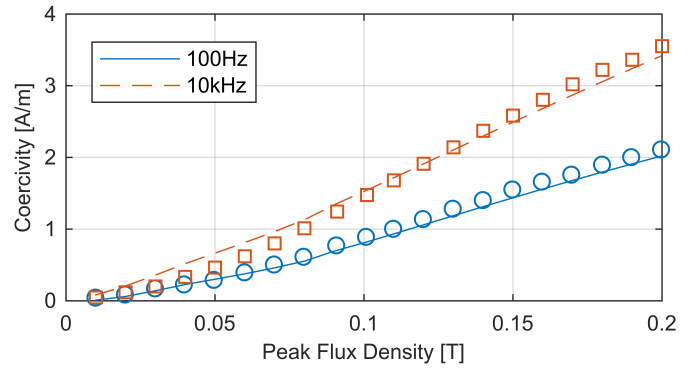

Fig. 18. Variation of T38 apparent coercivity with frequency

identifying the effective material conductivity from hysteresis loop measurements using the model of Section III. First, the low frequency hysteresis loops are identified. Next, a second set of measurements are taken at a frequency for which the apparent coercivity substantially increases. Then, starting with a nominal conductivity value, the model conductivity is adjusted so that the simulated high-frequency coercivity matches as near as possible the measured data. Fig. 18 shows the coercivity trend of the T38 core for two different frequencies over a range of flux densities.

References

[1] D. Jiles, *Introduction to Magnetism and Magnetic Materials*, 3rd ed. CRC Press, Sept 2015.
[2] A. Hubert and R. Schafer, *Magnetic Domains*. Springer, Nov 2008.
[3] G. Bertotti, *Hysteresis in Magnetism*. Academic Press, May 1998.
[4] J. B. Goodenough, "Summary of losses in magnetic materials," *IEEE Transactions on Magnetics*, vol. 38, no. 5, pp. 3398–3408, Sep 2002.
[5] I. Mayergoyz, *Mathematical Models of Hysteresis and Their Applications*. Academic Press, Aug 2003.
[6] D. C. Jiles, "Modelling the effects of eddy current losses on frequency dependent hysteresis in electrically conducting media," *IEEE Transactions on Magnetics*, vol. 30, no. 6, pp. 4326–4328, Nov 1994.
[7] H. Lamba, M. Grinfeld, S. McKee, and R. Simpson, "Subharmonic ferroresonance in an lcr circuit with hysteresis," *IEEE Transactions on Magnetics*, vol. 33, no. 4, pp. 2495–2500, Jul 1997.
[8] E. Barbisio, O. Bottauscio, M. Chiampi, G. Crotti, and D. Giordano, "Parameters affecting ferroresonance in lcr electric circuits," *IEEE Transactions on Magnetics*, vol. 44, no. 6, pp. 870–873, June 2008.
[9] M. Dimian, P. Andrei, O. Manu, and V. Popa, "Comparison of noise-induced resonance characteristics for different models of hysteresis," *IEEE Transactions on Magnetics*, vol. 47, no. 10, pp. 3825–3828, Oct 2011.
[10] ASTM A773 / A773M-01, "Standard Test Method for dc Magnetic Properties of Materials Using Ring and Permeameter Procedures with dc Electronic Hysteresigraphs", *ASTM International*, West Conshohocken, PA, 2001.
[11] IMA-STD-140, "Standard Specifications for Ferrite Toroid Cores", *The International Magnetics Association*, Cleveland, OH, 2011.
[12] J. N. Reddy, *An Introduction to the Finite Element Method*, 3rd ed. McGraw-Hill, 2006.
[13] J. W. Lu, S. Yamada, and H. B. Harrison, "Application of harmonic balance-finite element method (hbfem) in the design of switching power supplies," *IEEE Transactions on Power Electronics*, vol. 11, no. 2, pp. 347–355, Mar 1996.
[14] K. Geldhof, P. Sergeant, A. V. den Bossche, and J. Melkebeek, "Analysis of hysteresis in resonance-based position estimation of switched reluctance drives," *IEEE Transactions on Magnetics*, vol. 47, no. 5, pp. 1022–1025, May 2011.